Microporous and Mesoporous Materials 163 (2012) 85–95

Contents lists available at SciVerse ScienceDirect

Microporous and Mesoporous Materials

journal homepage: www.elsevier.com/locate/micromeso

Chromium and titanium/chromium-containing MCM-41 mesoporous silicates as promising catalysts for the photobleaching of azo dyes in aqueous suspensions. A multitechnique investigation

Verónica R. Elías [a,e], Ema V. Sabre [a], Elin L. Winkler [b,e], María L. Satuf [c,e], Enrique Rodriguez-Castellón [d], Sandra G. Casuscelli [a,e], Griselda A. Eimer [a,e,*]

[a] Centro de Investigación y Tecnología Química (CITeQ), Universidad Tecnológica Nacional, Facultad Regional Córdoba, Maestro López esq. Cruz Roja Arg. Ciudad Universitaria, 5016, Córdoba Capital, Argentina
[b] Centro Atómico Bariloche, CNEA-CONICET, Bustillo 9500, 8400 S.C. de Bariloche, Río Negro, Argentina
[c] INTEC, Universidad Nacional del Litoral-CONICET, Güemes 3450, (3000) Santa Fe, Argentina
[d] Departamento de Química Inorgánica, Cristalografía y Mineralogía, Facultad de Ciencias, Universidad de Málaga, Campus de Teatinos, 29071 Málaga, Spain
[e] CONICET: Consejo Nacional de Investigaciones Científicas y Técnicas, Argentina

ARTICLE INFO

Article history:
Received 12 April 2012
Received in revised form 13 June 2012
Accepted 23 June 2012
Available online 23 July 2012

Keywords:
Azo-dyes
Metallic species
Photobleaching
Biodegradability
MCM-41

ABSTRACT

Cr/MCM-41 and TiO_2/Cr/MCM-41 mesoporous silica were synthesized by the wet impregnation method. Scanning Electron Microscopy (SEM), Transmission Electron Microscopy (TEM), X-ray Photoelectron Spectroscopy (XPS) and Electron Spin Resonance (ESR) techniques were employed for the nanocatalysts characterization and a comparison with previously reported results of UV–Vis diffuse reflectance spectroscopy (UV–vis DR), X-ray Diffraction (XRD) and N_2 adsorption/desorption analysis was carried out. It could be confirmed that the lower Cr loadings in the samples result in the increased presence of highly dispersed oxidized Cr species, which allows the desired heterojunction effect after the Ti loading and the high catalytic activity in the Acid Orange 7 (AO7) degradation. In this work, the analysis of the AO7 degradation progress by UV–vis and FT-IR spectroscopy has been made using the TiO_2/Cr/MCM-41(3.5) as photocatalyst, under visible and UV–vis radiation. Short irradiation times resulted in a high degradation of the azo and naphthalene groups present in the AO7 dye. At longer irradiation times, when total discoloration of AO7 solution is obtained (>97%), the biodegradability index (BOD_5/COD) reaches values greater than 0.40. This photocatalytic process could be used as a pre-treatment step before conventional biological treatment.

© 2012 Elsevier Inc. All rights reserved.

1. Introduction

Due to the scarce freshwater resources, new tighter regulations concerning wastewater discharges have been established in many countries [1]. In this sense, the sustainable development became the main focus of the dialogue between the countries belonging to the United Nations (UN). Accordingly, there has been some progress on commitments to reconcile the economic activities with environmental protection [2]. On the other hand, industrial effluents of the textile industry are recognized as major pollutants due to the high amounts of water used during the dyeing operations [3–5]. Azo dyes represent the most significant group of dyes used in the industry today [5–7]. These compounds are widely used not only in textiles but also in the leather, paints and printing industries. In fact, they are chosen as coloring products due to their unique properties such as high wet strength and relatively low cost [8,9]. Due to their resistant to biodegradation, effluents containing azo dyes are hardly degraded by conventional biological methods [1]. Thus, Advanced Oxidation Processes (AOPs), particularly heterogeneous photocatalysis, have emerged as promising technologies to remove refractory pollutants from water due to their ability to use highly reactive hydroxyl radicals [10]. The initial step in the photocatalytic process involves the absorption of photons of suitable energy by the catalyst particles and the consequent generation of electrons and holes. These species can migrate to the particle surface and take part in oxidation–reduction reactions that can finally lead to the mineralization of the pollutants [1]. However, while AOPs allow the degradation of most refractory compounds, they can be expensive when they are compared to conventional biological treatments. Therefore, their use is more suitable when the solution to be treated is not easily biodegradable or when the amount of organic matter is low. An economically

* Corresponding author at: Centro de Investigación y Tecnología Química (CITeQ), Universidad Tecnológica Nacional, Facultad Regional Córdoba, Maestro López esq. Cruz Roja Arg. Ciudad Universitaria, 5016, Córdoba Capital, Argentina. Tel./fax: +54 0351 4690585.
E-mail address: geimer@scdt.frc.utn.edu.ar (G.A. Eimer).

1387-1811/$ - see front matter © 2012 Elsevier Inc. All rights reserved.
http://dx.doi.org/10.1016/j.micromeso.2012.06.043

viable option to treat wastewater containing nonbiodegradable pollutants consists in the combination of an AOP and a biological post-treatment. In this case, the chemical step is used to enhance the biodegradability of wastewater, so that it can be more easily treated biologically [11]. Besides, in order to design an efficient catalyst, it is very important to consider the properties that could affect the process development. Thus, it is of interest to synthesize materials with high surface area that can be used as a support of different photocatalytic species capable of working under visible light [12–14]. In this sense, the mesoporous molecular sieves MCM-41, have been extensively used as host porous structures [13,14]. Many transition metals oxides that absorb visible light could be loaded onto the surface of porous materials allowing a high dispersion of the active transition-metal species [12,13]. In previous work [15–17], we reported the modification of MCM-41 with different transition metals and their photocatalytic activity for the degradation of the azo-dye Acid Orange 7 (AO7). It was shown that using visible light, only the materials modified with Cr present high AO7 decolorization levels. Even though Cr modified mesoporous materials have been the subject of several literature reports [18–20], thorough and systematic investigations on the nature of the Cr species in terms of the Cr loading and its influence on the photocatalytic activity are scarce. A complete characterization of different Cr species requires the combination of spectroscopic techniques. In the present work, we investigated in detail the nature of the Cr species formed on these mesoporous silicates and their interaction with loaded Ti species. Additionally, the progress of the photocatalytic degradation of AO7 under visible and UV–vis light was analyzed by studying the time-dependent UV–vis and FT-IR spectral changes. Moreover, changes in the biodegradability of the reaction solution were also analyzed.

2. Experimental procedures

2.1. Synthesis

The metal-free MCM-41 mesoporous molecular sieve was synthesized as previously reported [21], using cetyltrimethylammonium bromide (Merck 99%) as template and tetraethoxysilane (Aldrich 98%) as silicon source (method B in reference [21]). The synthesis mixture (pH 11.25) was stirred at room temperature for 4 h. Then, this gel was heated at 343 K under stirring in a closed flask. The Cr modified MCM-41 materials were prepared by the wet impregnation method as reported in our earlier work [15] using $Cr(NO_3)_3{\cdot}9H_2O$ (Anedra 98%) as Cr precursor. The used amount of this salt was the corresponding one to achieve a loading of 10.00, 5.00, 3.50, 1.50 and 0.75 wt.%. The resulting powder was dried at 333 K and calcined for 9 h at 773 K. Then, these solids were also modified by TiO_2 loading using a 3.2 wt.% of titanium *n*-butoxide (Fluka 97%) solution in isopropanol (Cicarelli 99.5%). The materials were named: Cr/MCM-41(x) or TiO_2/Cr/MCM-41(x), where x indicates the theoretical loading of Cr.

2.2. Characterization

The materials were characterized by XRD, UV–vis DR and N_2 adsorption according to [17]. Here, X-ray photoelectron spectra were collected using a physical electronics PHI 5700 spectrometer with non-monochromatic Mg Kα radiation (300 W, 15 kV, 1253.6 eV) for the analysis of photo-electronic signals of C 1*s*, O 1*s*, Si 2*p*, Ti 2*p* and Cr 2*p* and multichannel detector. Spectra of powdered samples were recorded with the constant pass energy values at 29.35 eV, using a 720 μm diameter analysis area. During data processing of the XPS spectra, binding energy values were referenced to the C 1*s* peak (284.8 eV) from the adventitious contamination layer. The PHI ACCeSS ESCA-V6.0 F software package was used for acquisition and data analysis. A Shirley-type background was subtracted from the signals. Recorded spectra were always fitted using Gauss-Lorentz curves, in order to determine the binding energy of the different element core levels more accurately. The error in the binding energy (BE) was estimated to be ca. ±0.1 eV. ESR spectra of calcined samples at 773 K were recorded with a Bruker ESP 300 spectrometer at 9.5 GHz in the 110–300 K temperature range. SEM micrographs were obtained in a JEOL model JSM 6380 LV, working voltage: 20 kV. Lower resolution TEM images were obtained in a JEOL Model JEM-1200 EXII System, working voltage: 120 kV.

2.3. Catalytic experiments

The degradation experiments were performed with a photoreactor as it was described elsewhere [15–17] using four UV–vis lamps (Actinic BL 20 W, Philips) as a source of light. The concentration (C) of AO7 was monitored using Jasco V 650 spectrophotometer by measuring the absorbance at $\lambda = 485$ nm assigned to the hydrazone form of the dye. The cleavage of the –N=N– bond leads to decolorization of the solution. Therefore the decolorization percentage was calculated as $X = (C_0 - C) \times 100/C_0$ [16,17]. The progress of the photocatalytic process was made by FT-IR spectroscopy using a Jasco 5300. Samples for FT-IR analyses were prepared evaporating the solution at 50 °C under reduced pressure in presence of KBr used as a solid support. The mineralization degree of AO7 was measured from the Total Organic Carbon (TOC) concentration changes using a TOC/TNB Analyzer Vario TOC cube. The mineralization efficiency was defined by the following equation: $(TOC_0 - TOC) \times 100/TOC_0$, where TOC is the value of TOC obtained at time *t* and TOC_0 correspond to the initial value of TOC. The chemical oxygen demand (COD) measurements were obtained by following the closed reflux, colorimetric method [22]. The 5-days biochemical oxygen demand assay (BOD_5) was employed to evaluate changes in the biodegradability of the samples, employing the respirometric method [22] with a BOD System (Velp Scientifica) and PolySeed® inoculum (Interlab®).

3. Results and discussion

3.1. Structural characterization

The characterization results by XRD and N_2 adsorption of the synthesized catalysts were presented by us elsewhere [17]. Here, measurements of transmission electron microscopy of the calcined materials were made in order to examine their structural regularity. TEM images of the pure siliceous MCM-41 and TiO_2/MCM-41 samples are shown in Fig. 1. MCM-41 sample presents a well-defined mesoporous structure (Fig. 1(a)), exhibiting well ordered parallel straight mesochannels characteristic of the hexagonal pore arrangement of MCM-41 type materials [23], which was also observed by us in the XRD patterns [17]. The average mesopore size estimated by TEM is around 2.5 nm which is in agreement with the values determined from adsorption data [17]. It should be noted that in Fig. 1(a) the image is viewed perpendicularly to the direction of the hexagonal pore arrangement [24], clearly showing the presence of straight mesochannels arraying along the long axis [25]. Then, the image corresponding to TiO_2/MCM-41 is similar to MCM-41 sample (Fig. 1(c)), in the periodicity of the hexagonal mesopore arrangement. Nevertheless, after the loading with titania, it is noteworthy that there were segregated TiO_2 particles on the external surface of silicate. This result is expected for materials modified with transition metals prepared via wet impregnation [26–31]. In fact, Fig. 1(b) and (c) show small TiO_2 particles which

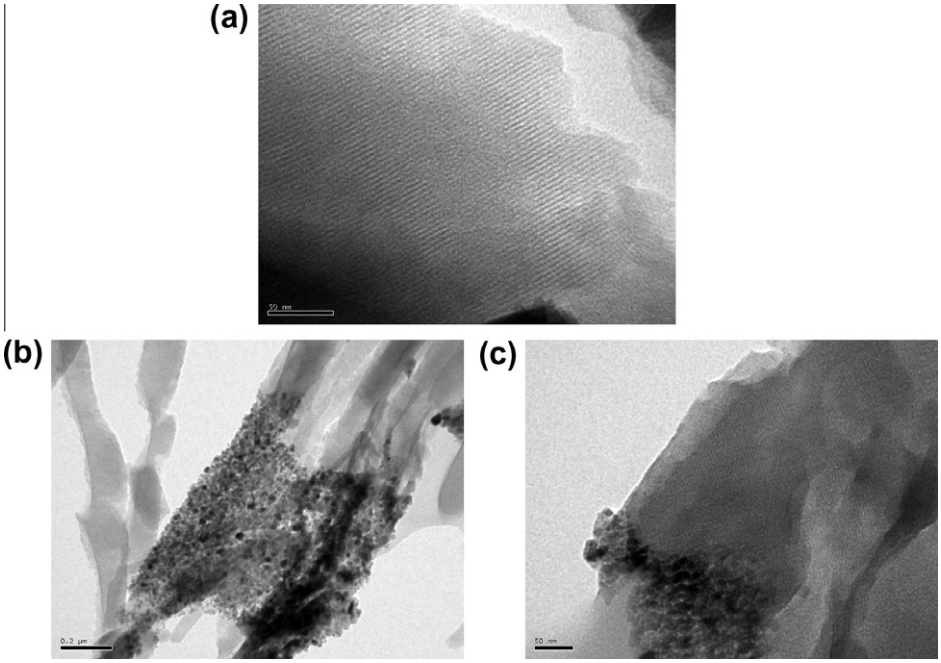


Fig. 1. Transmission electron microscopy images: (a) MCM-41, (b)-(c) TiO_2/MCM-41.

are decorated on the external surface of the MCM-41 support and are slightly agglomerated. Nevertheless, the image in Fig. 1(b) shows TiO_2 particles more uniformly dispersed with sizes from 15 to 25 nm. The above results are basically consistent with those estimated from XRD data [17]. Moreover, in Fig. 1(c) it can be observed the regular and ordered straight channel characteristics of MCM-41 which are preserved as domains of hexagonally ordered mesopores, unaffected by the presence of TiO_2 particles [32]. It is important to note that with TEM it could be observed particles of small size that cannot be observed by XRD. Additionally, non-crystalline species could also be observed by this technique [33]. TEM images of the Cr/MCM-41(3.5) and Cr/MCM-41(10) samples are presented in Fig. 2(a) and (b), respectively. It is observed that the hexagonal pore arrangement of the MCM-41 host is maintained after the Cr loading. Since the darker area in TEM images represents the electronically more dense phases, metal oxide is considered to be present when irregular contrasts in the images are observed [34]. Thus, a few high-contrast regions randomly that interrupt the pore arrangement, corresponding to a scarce number of Cr_2O_3 segregated particles, are observed for Cr/MCM-41(3.5)

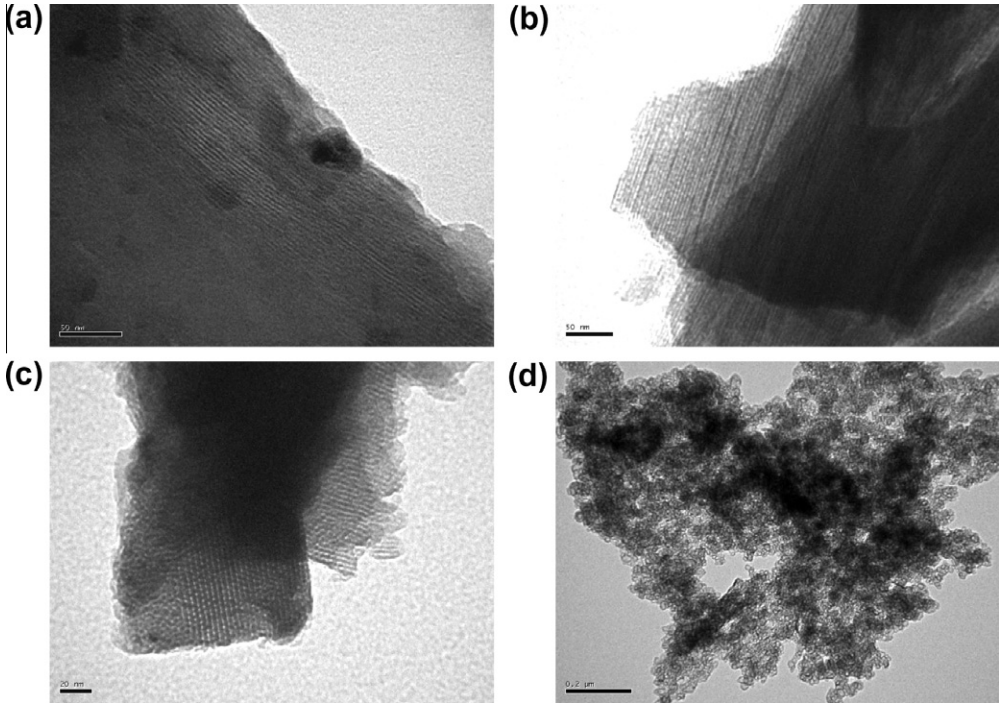


Fig. 2. Transmission electron microscopy images: (a) Cr/MCM-41(3.5), (b) Cr/MCM-41(10), (c)–(d) TiO_2/Cr/MCM-41(3.5).

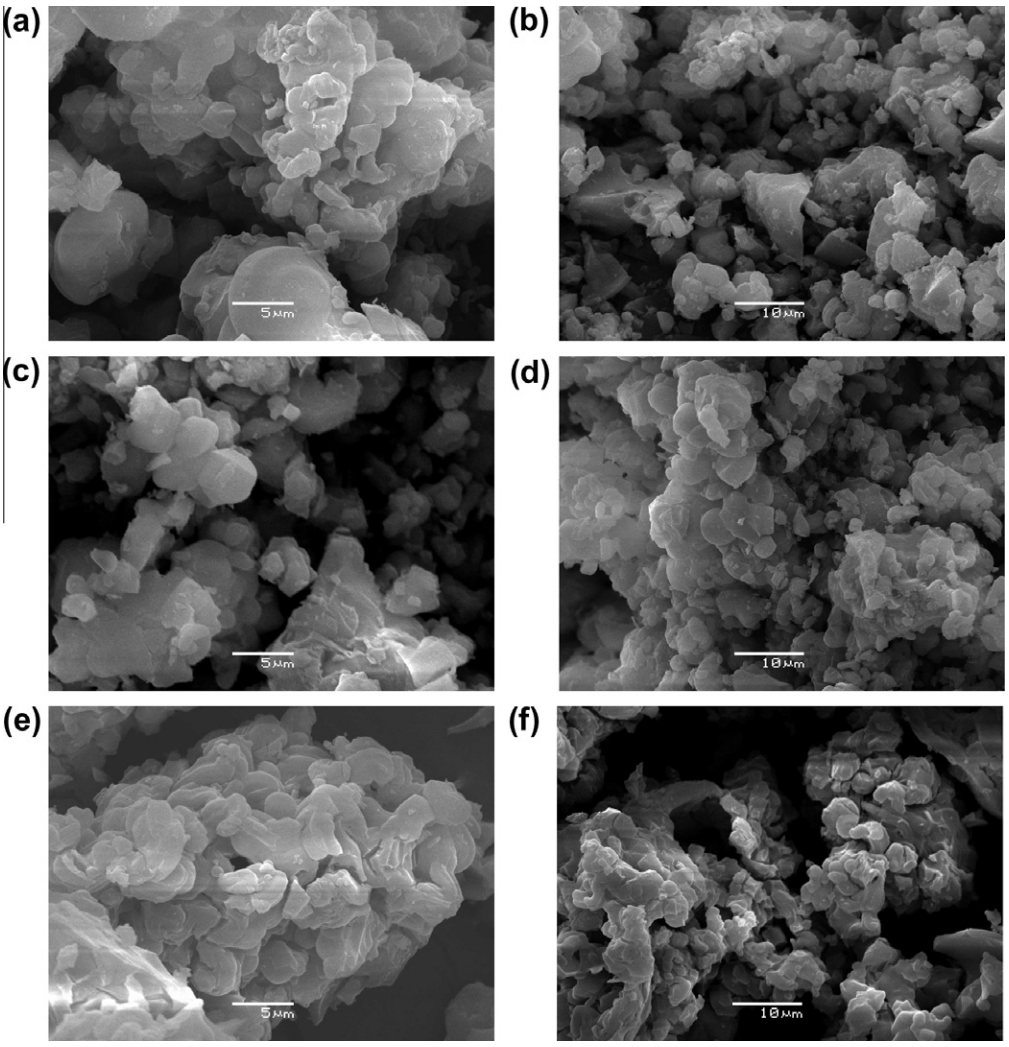


Fig. 3. Scanning electron micrographs of: (a)–(b) Cr/MCM-41(3.5), (c)–(d) Cr/MCM-41(10), (e)–(f) TiO_2/Cr/MCM-41(3.5).

sample. The estimated size of these particles is around 10 nm, which is hardly detected by XRD [28,35,27]. For its part, the Cr/MCM-41(10) sample presents a lack of these regions in its TEM image, although the XRD analysis revealed the presence of large oxide particles [17]. However, the small amount of these large particles could be the reason why these were not observed by TEM [30,35,27]. Besides, the incorporation of the chromium oxide inside the mesoporous channels could be confirmed by TEM micrograph in the Cr/MCM-41(10) sample. In fact, the impregnation with a high amount of Cr nitrate and the calcination at 773 K, results in the formation of clusters or very small particles of oxide within the mesoporous silica channels evidenced by the darker regions along the mesopores (Fig. 2(b)) [36]. The TEM images of the TiO_2/Cr/MCM-41(3.5) sample are presented in Fig. 2(c) and (d). The regular and ordered straight-channels characteristics of MCM-41 can be observed on the edges of the image in Fig. 2(c). This is consistent with the low-angle XRD results presented by us elsewhere [16,17]. Moreover, in this figure, the pores seem to be filled with the metallic oxides judging by the very small darker regions of around 1.5 nm, which is evidence for incorporation of the titanium species. Nevertheless, in the Fig. 2(d) TiO_2 particles bigger than 25 nm were observed. The estimation of particle size from the TEM image is in good agreement with that calculated by using the Scherrer's equation [17]. Additionally, the aggregation of the TiO_2 particles is also notable for this sample (Fig. 2(d)). On the other hand, the particle size and morphology of synthesized samples were also investigated by scanning electron microscopy. The SEM images of the Cr/MCM-41(3.5) and Cr/MCM-41(10) samples are shown in Fig. 3(a–d). These images indicate the presence of particles that do not display any particular crystalline habit or morphology, although the spherical-like morphology seems to be the dominant one. The primary particles are very small and appear to be aggregated into larger secondary particles which exist in various sizes (~5–8 μm). These apparent single particles observed in the SEM could be the result of intergrowth of multiple smaller particles [37]. Partial aggregation was observed after the Ti loading on the Cr/MCM-41(3.5) sample (Fig. 3e–f). Thus, their SEM micrographs show agglomerates of irregular morphology as short banana-like rods [38]. This morphology is possibly due to that the metallic oxides are deposited at different locations provoking the agglomeration [39]. It is noteworthy that exists a substantial amount of fragments in the final Cr/MCM-41(x) and TiO_2/Cr/MCM-41(3.5) samples, possibly due to the incorporation method of the metallic oxide species on the MCM-41 support. Nevertheless, all these samples exhibit a very well-resolved X-ray diffraction patterns [16,17]. Therefore, it will be expedient to independently optimize the particle morphology and the mesoporous structure characteristic of MCM-41 materials [40].

3.2. Spectroscopic characterization

The coordination environmental of the metallic species in the MCM-41 structure was studied by UV–vis DR and presented in [17]. In this work, the XPS analysis has been employed to obtain information concerning the superficial composition of catalysts, the chemical state of the constituent elements and the chromium dispersion. The Si 2*p* binding energy value for all of the samples is around 103.4 eV, which is characteristic of MCM-41 silica. The binding energy values of the core level O 1*s* and Cr 2*p* signals are shown in Table 1. As it can be observed in this Table, the photoemission O1*s* for the samples Cr/MCM-41(x) is mainly due to the contribution of oxygen from silica. Only for the sample Cr/MCM-41(10) this signal becomes asymmetric due to the overlapping of the contribution of oxygen from silica and from chromium oxide. The TiO_2/Cr/MCM-41(x) samples showed three contributions of the O1*s* binding energy values around 529.8, 532.0 and 533.4 eV (see Table 1) and belong to the oxygen atoms from CrO_x, TiO_2 and SiO_2. The area percentage of the O1*s* contribution corresponding to SiO_2 is drastically reduced when titania was loaded on the Cr/MCM-41(x) samples. This fact indicates that the Ti loading changes the surface composition of the samples and could also cause a possible oxygen atoms migration. On the other hand, Table 1 lists the surface Cr/Si and Cr/Ti atomic ratios determined by XPS and the bulk Cr/Si ratio determined by XRF (X-ray Fluorescence) for all of the synthesized catalysts. Generally, the surface Cr/Si atomic ratio can be considered as the relative dispersion of transition metal ions on the structure of porous supports [19]. In this sense, the values of this ratio were compared with the bulk Cr/Si ratios [19]. For the Cr/MCM-41(x) samples, the surface Cr/Si atomic ratio increases with an increase in the bulk Cr/Si ratio in the catalyst. However, for the higher loaded samples, this surface Cr/Si ratio is notably lower than the corresponding bulk Cr/Si ratio, indicating that the Cr atoms would be mostly incorporated inside the mesopores. The surface Cr/Si ratios for the Cr/MCM-41(x) samples are smaller than those for the TiO_2/Cr/MCM-41(x). These results could be due to the enhancement of the surface mobility, surface arrangement and segregation of chromia onto the surface caused by the migration of extraframework chromium away from the TiO_2/Cr/MCM-41(x) interface after the titania loading. On the other hand, for these samples, the general trend is an increase in the Cr/Si surface ratio according to the incremented bulk Cr/Si ratio. Nonetheless, above the theoretical loading of 3.5 wt.% a notable decrease in the surface Cr/Si ratio is observed. This fact could be giving account for the heterogeneous character of catalyst as a consequence of the migration of surface Cr species and formation of nano-particles of α-Cr_2O_3 as a segregated phase. The Cr 2*p* core level photoelectron profiles for all of the synthesized samples are shown in Fig. 4. The samples with a low Cr-content shows two different Cr species or chemical states on these catalyst surfaces. The lowest binding energy contribution around 576.5 eV is assigned to Cr^{3+} and the highest binding energy contribution at around 579.5 eV corresponds to Cr^{6+}. With respect to the Cr/MCM-41(x) samples, only the Cr/MCM-41(0.75) and Cr/MCM-41(1.5) samples present Cr^{6+} species on the surface, although the existence of Cr^{6+} has been corroborated by UV–vis DR spectroscopy for all of the samples. According to the literature, for similar materials, the contribution of surface Cr^{6+} decreases with the Cr content [19,41–43]. Therefore, it is reasonable that the only chromium species on the surface of the higher Cr loaded samples is Cr^{3+}. Finally, after the Ti loading, the Cr 2*p* core level spectrum of the TiO_2/Cr/MCM-41(0.75) sample is the only one that shows the presence of surface Cr^{6+} species.

The ESR spectroscopy is a very sensitive technique to study the nature and the crystal symmetry environment of different magnetic ions into the molecular sieves, besides it can provide complementary information to that obtained by UV–vis DR and XPS spectroscopy. As it is well known, the electron structure of the transition metal ions is modified by the electric field derived from the neighboring atoms. For example, in an octahedral symmetry site, the fivefold d-orbital degeneracy is splitted into triplet t_{2g}-orbitals and doublet e_g-orbitals. For the particular case of chromium ions located in an octahedral symmetry site, the corresponding electronic configurations are: Cr^{3+}, $3d^3$ ($t_{2g}^3 \cdot e_g^0$) S = 3/2; Cr^{5+}, $3d^1$ ($t_{2g}^1 \cdot e_g^0$) S = 1/2 and Cr^{6+}·$3d^0$ ($t_{2g}^0 \cdot e_g^0$) S = 0. The Cr^{3+} and Cr^{5+} ions in the paramagnetic state are easily detected by ESR. Instead, the Cr^{6+} is diamagnetic and, hence, is not detectable by ESR spectroscopy. Therefore, from the ESR spectra, the nature and the symmetry of the chromium ions into the molecular sieves could be inferred.

Fig. 5A shows the ESR spectra of the Cr/MCM-41(x) samples. From these measurements two different signals are observed. One of the ESR lines, identified as γ, is centered at Hr $\sim$ 3400 Gauss and presents a peak to peak linewidth (ΔH_{pp}) of approximately 20 Gauss. The second ESR line, identified as β, is inhomogeneously broadened with a ΔH_{pp} of around 800–1000 Gauss and it is centered at Hr $\sim$ 3400 Gauss. The γ signal is present in all of the spectra of the Cr/MCM-41(x) samples after the calcination process in air atmosphere. Fig. 6 shows a detail of this absorption where an asymmetric lineshape is observed. This spectrum can be described by a spin Hamiltonian that takes into account the Zeeman interaction. This term describes the interaction of an S = 1/2 spin with the magnetic field: $H = \mu_B \cdot H \cdot g \cdot S$, where μ_B is the Bohr magneton, g is the gyromagnetic tensor. Assuming a distorted octahedral site with tetragonal symmetry, the principal values of the g-tensor are $g_x = g_y = g_\perp$ $g_z = g_{//}$. As the studied samples are in powder form,

Table 1
XPS binding energy values and Surface atomic concentration of Cr/MCM-41(x) and TiO_2/Cr/MCM-41(x) samples.

Sample	Cr $2p_{3/2}$ BE[a] (eV)		O 1*s* BE (eV) [a]			Cr bulk (%*p*/*p*) (XRF)	Cr (%at.) (XPS)	Cr/Si bulk atomic ratios (XRF)	Surface atomic ratios	
	Cr^{6+}	Cr^{3+}	CrO_x	TiO_2	SiO_2				Cr/Si	Cr/Ti
Cr/MCM-41(0.75)	579.7 (46)	576.8 (54)	–	–	532.9	0.478	0.57	0.0129	0.018	–
Cr/MCM-41(1.5)	579.7 (29)	576.1 (71)	–	–	532.8 (100)	0.890	0.73	0.0243	0.023	–
Cr/MCM-41(3.5)	–	577.2 (100)	–	–	533.1 (100)	2.048	0.89	0.0563	0.028	–
Cr/MCM-41(5)	–	576.5 (100)	–	–	532.8 (100)	2.897	0.87	0.0831	0.027	–
Cr/MCM-41(10)	–	576.2 (100)	530.3 (5)	–	533.1 (95)	6.506	1.69	0.1873	0.055	–
TiO_2/MCM-41	–	–	–	530.1 (39)	533.2 (61)	–	–	–	–	–
TiO_2/Cr/MCM-41(0.75)	579.5 (15)	576.5 (85)	529.8 (51)	532.1 (23)	533.5 (26)	0.266	3.72	0.0091	0.316	0.365
TiO_2/Cr/MCM-41(1.5)	–	577.0 (100)	529.8 (47)	531.9 (13)	533.3 (40)	0.545	15.88	0.0189	1.093	1.918
TiO_2/Cr/MCM-41(3.5)	–	576.7 (100)	529.7 (72)	531.8 (15)	533.3 (13)	1.336	10.41	0.0471	2.974	0.854
TiO_2/Cr/MCM-41(5)	–	576.6 (100)	529.9 (47)	532.1 (23)	533.5 (30)	1.824	6.38	0.0641	0.331	0.862
TiO_2/Cr/MCM-41(10)	–	577.1 (100)	529.9 (58)	532.1 (21)	533.4 (21)	3.455	6.03	0.131	0.359	0.628

[a] Between brackets figure the corresponding species percentage.

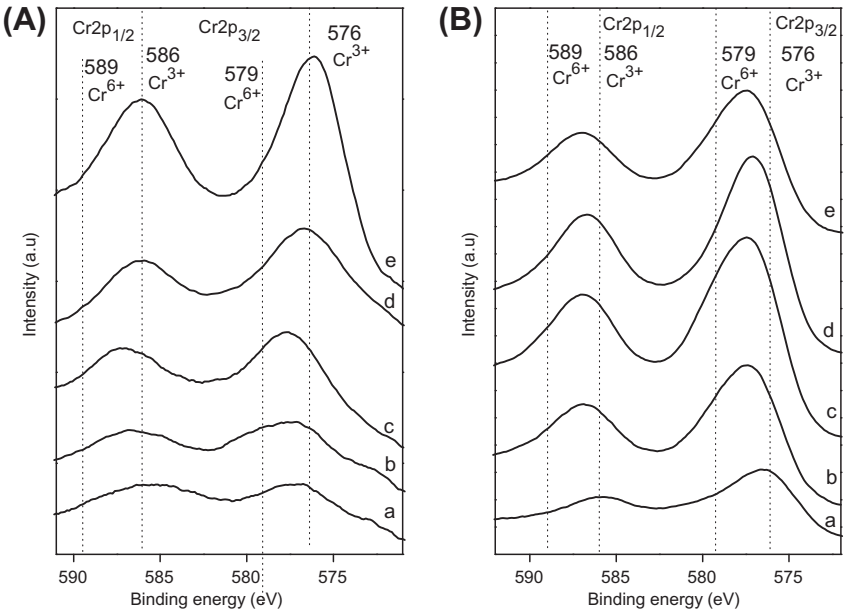


Fig. 4. Cr 2*p* core level photoelectron profile of A) (a) Cr/MCM-41(0.75), (b) Cr/MCM-41(1.5), (c) Cr/MCM-41(3.5), (d) Cr/MCM-41(5), (e) Cr/MCM-41(10) and B) (a) TiO_2/Cr/MCM-41(0.75), (b) TiO_2/Cr/MCM-41(1.5), (c) TiO_2/Cr/MCM-41(3.5), (d) TiO_2/Cr/MCM-41(5), (e) TiO_2/Cr/MCM-41(10).

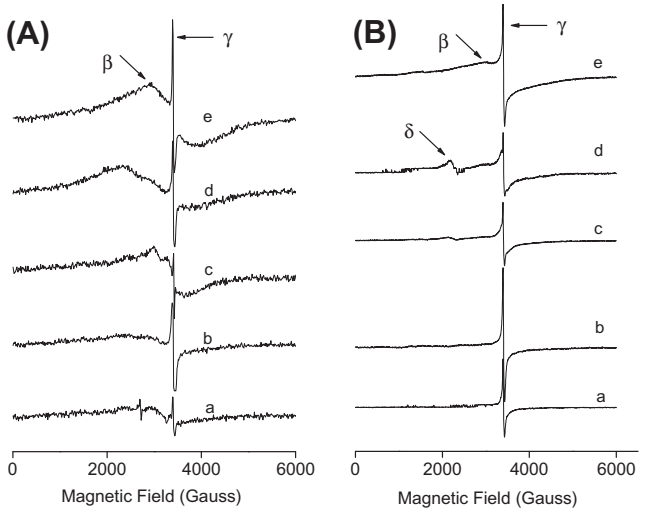


Fig. 5. ESR spectra of A) (a) Cr/MCM-41(0.75), (b) Cr/MCM-41(1.5), (c) Cr/MCM-41(3.5), (d) Cr/MCM-41(5), (e) Cr/MCM-41(10) and B) (a) TiO_2/Cr/MCM-41(0.75), (b) TiO_2/Cr/MCM-41(1.5), (c) TiO_2/Cr/MCM-41(3.5), (d) TiO_2/Cr/MCM-41(5), (e) TiO_2/Cr/MCM-41(10).

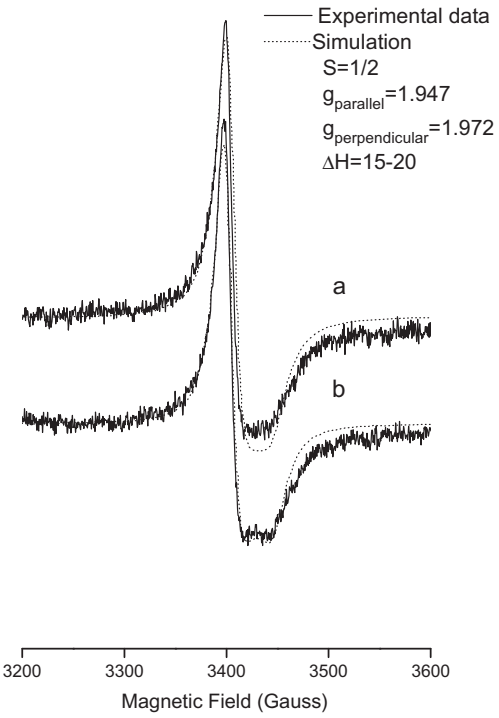


Fig. 6. Evolution of the γ signal in the ESR spectra of the samples (a) Cr/MCM-41(10) and (b) Cr/MCM-41(1.5).

the ESR line results from the contribution of the spectra corresponding to all of the possible space directions. Therefore, assuming homogeneous angular distribution of the symmetry axis, a powder spectra simulation was performed. Fig. 6 shows representative simulations obtained considering $g_{//} = 1.947$ and $g_{\perp} = 1.972$ with a peak to peak linewidth $\Delta H_{pp} \sim 20$ Gauss. The obtained parameters are consistent with mononuclear Cr^{5+} species [44,45].

On the other hand, the second signal in the spectra centered at $g \sim 1.96$ is denominated β and decreases when the Cr content diminishes. In fact, the β signal is not detected in samples with lower Cr loadings (Cr/MCM-41(1.5) and Cr/MCM-41(0.75)). In order to confirm the origin of the ESR resonance we have performed measurements as a function of the temperature. Fig. 7 shows the evolution with the temperature of the ESR spectra for the Cr/MCM-41(10) sample. From this figure it can be observed that the β-linewidth increasesand the ESR intensity (I_{ESR}) decreases when the measurement temperature diminishes. Fig. 8 shows the evolution of the ESR intensity (calculated as $\Delta H_{pp}{}^2 h_{pp}$, where h_{pp} is the peak to peak height) with the temperature. From the ESR parameters and their evolution with the temperature, we ascribed this resonance to Cr_2O_3-like clusters [46]. It is known that the bulk Cr_2O_3 orders antiferromagnetically (AFM) below the Néel temperature $T_N = 308$ K. Therefore, above T_N a paramagnetic resonance is observed, instead below T_N, large anisotropy and exchange fields

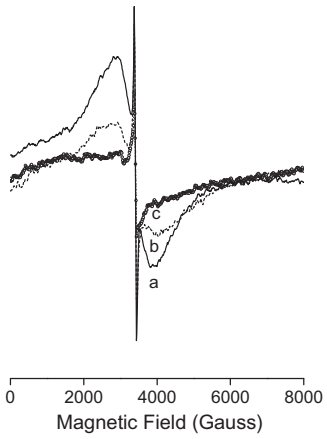


Fig. 7. Evolution of the β signal in the ESR spectra of the Cr/MCM-41(10) sample measured at: (a) 288 K, (b) 220 K, (c) 145 K.

are present so the resonant mode could not be excited [47]. When the size of the Cr_2O_3 is reduced to nanometer scale, it was observed that T_N shifts to lower temperature and the AFM transition is developed in a wider temperature range [48,49]. Moreover, the ESR signal is still observed below T_N as a consequence of the surface disorder. Therefore, the temperature dependence of the β-signal is consistent with the expected behavior of AFM Cr_2O_3 clusters. The obtained ESR parameters are also consistent with the XRD and UV–vis DR results [17] that indicate a decrease in the amount and size of Cr_2O_3 nanoparticles when the Cr loading diminishes.

As it was mentioned above, from the ESR spectroscopy the Cr^{3+} and Cr^{5+} ions can be detected. Besides, the ESR intensity is proportional to the number of resonant ions. Therefore, if all of the chromium ions in the sample are reduced to Cr^{3+}, we could quantify the concentration of chromium and calculate the initial proportion of Cr^{3+}, Cr^{5+} and Cr^{6+} ions in the catalyst. With this objective in mind, some of the samples were subject to a reduction treatment at 600 °C for 6 h under H_2 flow (10 °C/min). Fig. 9A shows the ESR spectra of the Cr/MCM-41(3.5) before and after the thermal treatment. After the reduction, a remarkable enhancement of the signal is observed; this result indicates the increase of the resonant magnetic species after the treatment. Moreover, the γ signal (assigned to Cr^{5+}) disappears which is in agreement with the reduction the chromium species to the lower oxidation state (Cr^{3+}), this behavior was already observed by Cordischi et al. [50]. In order to quantify the different oxidation states of chromium, we have assumed that after the thermal treatment in H_2 atmosphere all of the ions were reduced to Cr^{3+}. Therefore, from the comparison of ESR intensity of Fig. 9 A we could estimate the initial distribution of Cr^{6+}, Cr^{5+} and Cr^{3+} ions as 80 ± 8%, 0.2 ± 1% and 20 ± 8%, respectively. In addition, the ESR spectrum of the reduced Cr/MCM-41(3.5) sample is similar to that observed by Tobia et al. [48] for α-Cr_2O_3 nanoparticles. Nevertheless, the temperature dependence of the ESR intensity follows a different behaviour: the I_{ESR} slightly increases when the temperature diminishes (Fig. 10). This result implies that this signal cannot be assigned to crystalline chromia which presents long range AFM order; instead it can be assigned to isolated Cr^{3+} into the sieve or amorphous Cr_2O_3 clusters. This result agrees with the XRD analysis of the reduced sample which does not show peaks corresponding to the α-Cr_2O_3 phase and with the UV–Vis DR spectra analysis that shows increasing presence of Cr^{3+} oxide clusters after the reduction treatment [17]. Similar results were observed by Puurunen et al. [46] in ruby-type chromia/alumina samples where isolated Cr^{3+} ions are located inside alumina.

Fig. 5 B shows the ESR spectra corresponding to the TiO_2/Cr/MCM-41(x) samples. From this figure it is also observed a thin line ($\Delta H_{pp} \sim 35$ Gauss) centered at $g = 1.969(2)$ and a broad line ($\Delta H_{pp} \sim 900$ Gauss) centered at $g = 1.97(2)$ identified as γ and β, respectively. It is noteworthy that for the lower Cr loadings the β signal is not observed. Besides, a weak line at higher g values ($g \sim 3$) is observed in the spectra corresponding to the TiO_2/Cr/MCM-41(5) and TiO_2/Cr/MCM-41(3.5) samples. This signal is ascribed to surface isolated Cr^{3+} ions located in low symmetry crystal sites and it is denoted as δ phase [46,51]. The coordination environment of the surface Cr^{3+} species may change in the different samples. In this sense, Cr^{3+} at low symmetry sites can be stabilized after the titania coverage. Nevertheless, the number of sites where Cr^{3+} can be stabilized in isolated positions is practically constant for a given support [38,46,52–54]. As a consequence, a marked increase in the Cr loading could result in a further decrease in the amount of isolated Cr^{3+} sites due to its aggregation and consequent formation of large Cr_2O_3 clusters. This fact could be the reason because the TiO_2/Cr/MCM-41(10) sample did not show δ signal. Instead, for the samples with lower Cr loadings, the higher concentration of isolated Cr^{3+} ions in the surface originates the δ signal. When the Cr loading is very small, the low content of the Cr^{3+} ions results in a broadened signal beyond the detection limit.

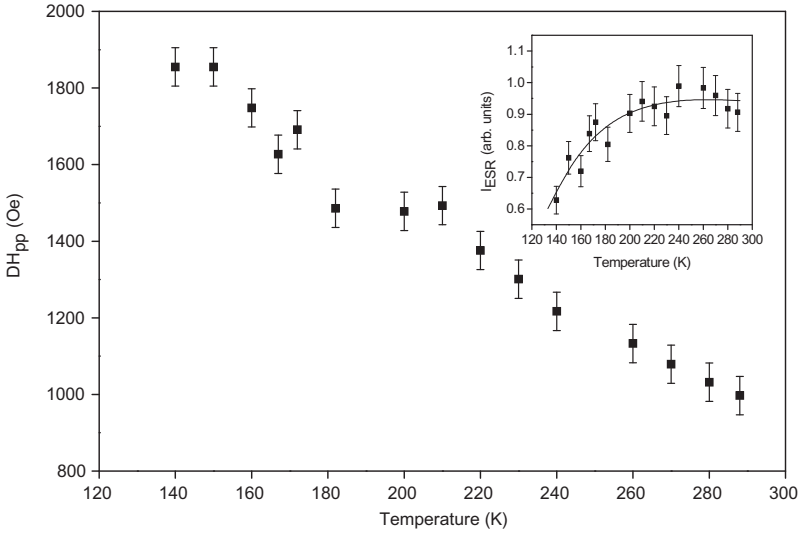


Fig. 8. ΔH_{pp} vs T for the sample Cr/MCM-41(10). Inset: ESR intensity as function of temperature.

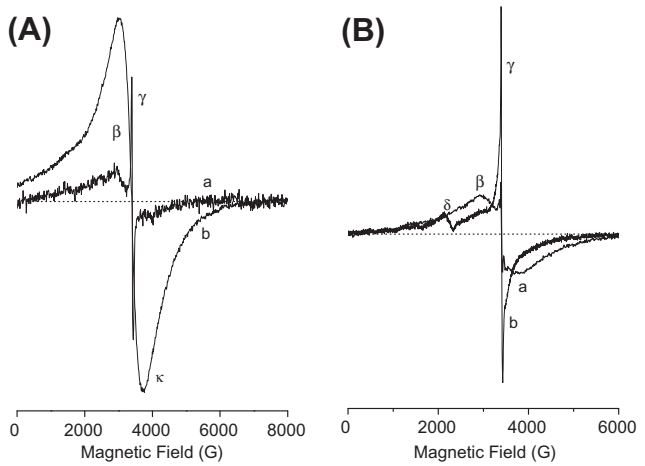


Fig. 9. A) ESR spectrum of the sample Cr/MCM-41(3.5) before (a) and after (b) the reduction treatment and B) EPR spectrum of the sample TiO_2/Cr/MCM-41(3.5) before (a) and after (b) the reduction treatment.

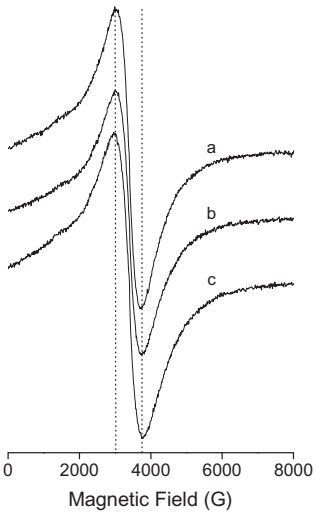


Fig. 10. ESR spectrum Cr/MCM-41(3.5) Reduced sample measured at: (a) 297 K, (b) 220 K, (c) 145 K.

In order to evaluate the evolution of the magnetic ions after the thermal treatment in reducing atmosphere the TiO_2/Cr/MCM-41(3.5) sample was subjected to a reduction treatment at 600 °C for 6 h under H_2 flow (10 °C/min). Fig. 9 B compares the ESR spectra measured before and after the reduction treatment. It is notorious that the β signal increases after the reduction, which evidences the increment of the proportion of Cr^{3+}. Nevertheless, although the ESR intensity of the β signal increases, unlike to the Cr/MCM-41(3.5) sample, the γ line is still present after the reduction. This result evidences that, not all of the chromium ions could be reduced to Cr^{3+}, as a consequence we could not quantify the initial proportion of chromium species. In addition, this result is a further evidence of the shielding effect of the titania on the oxidized-Cr species.

3.3. Photodecolorization of AO7

In previous works we studied the photodegradation of AO7 using several MCM-41 molecular sieves loaded with different transition metals (Cr, Fe, Co) and then loaded with Ti, under visible and UV–vis light [15,16]. Under visible light, it was found that the TiO_2/Cr/MCM-41(x) samples reached the higher degradation rates. In other work [17], we could relate the photocatalytic activity of the Cr modified MCM-41 with the presence of Cr^{6+} species. This activity steadily increased with increasing Cr loading up to a 3.50 wt.%. Meanwhile, a further increase in this loading just allowed slightly enhancing the activity, which could be explained by the incremented presence of inactive Cr^{3+} species (clusters and α-Cr_2O_3 nano-particles), observed by XRD and UV–vis DR [17] and confirmed here by the XPS and ESR analysis. In addition, the ESR results for the Cr/MCM-41(3.5) reduced sample showed here, allowed us to confirm that the Cr^{3+} species, arising from the reduction process, are responsible for the lack of activity observed in [17]. On the other hand, in the case of the TiO_2/Cr/MCM-41(x) catalysts, a synergistic effect between the Cr and Ti species was observed for theoretical Cr loadings up to 3.50 wt.% [17]. Then, the non-increased photoactivity for the highest Cr loadings samples when TiO_2 was loaded was related to the presence of clusters or large oxide particles of Cr^{3+}, that avoid the diffusion of Ti species into the channels and its interaction with Cr^{6+}. Finally, given that the TiO_2/Cr/MCM-41(3.5) sample appeared as optimal due to its high catalytic performance ($X \sim 80\%$ under 5 h of visible irradiation) and its high stability to leaching [17], this sample was chosen for the AO7 degradation experiments carried out in this work.

The progress of the reaction was analyzed by studying the time-dependent UV–vis spectral changes during the photocatalytic degradation of AO7 (Fig. 11). The original absorption of AO7 mainly consists of three well-resolved peaks at 485, 311 and 230 nm and two shoulders at 254 and 430 nm. In the visible region, the absorptions at 485 and 430 nm are assigned to the hydrazone and azo forms of AO7, respectively. These forms originate from intermolecular hydrogen bonding tautomeric interactions between the oxygen of the naphthyl group and the β-hydrogen of the corresponding azo-linkage, respectively (inset Fig. 11A) [55,56] and, in aqueous solution, the two forms are in equilibrium. The other absorption peaks in the UV region, at 230 and 311 nm are ascribed to π–π^* transitions in the benzene and naphthalene rings of AO7, respectively [57–59]. After the addition of the catalyst and upon reaching equilibrium in the dark, the absorbance decreases reflecting the extent of the AO7 adsorption on the photocatalyst surface. As it was explained elsewhere [17], the decrease in the AO7 concentration in the dark depends on the Cr-loading in the catalyst. A decrease in the AO7 absorbance of about 21% was observed when TiO_2/Cr/MCM-41(3.5) sample was used as photocatalyst. The UV–vis spectral changes under *visible* light are shown in Fig. 11 A. It is clear that the absorption at 230, 311 and 485 nm decreases with time and a decolorization of around 80% was reached after 5 h of reaction resulting in an almost complete degradation of the intermediates containing naphthalene rings. The same trend was observed for the reaction under UV–vis light (Fig. 11B), although the decolorization was faster than when visible light was used. The normalized absorbances at 485, 311 and 230 nm are plotted against the irradiation time for the experiments carried out under visible and UV–vis light (Fig. 12). It is observed that the intensity of the band corresponding to the azo-linkage (AO7) decreases with the time and practically disappears ($X > 97\%$) after 20 h for visible irradiation and 10 h for UV–vis irradiation (Fig. 12A and B, respectively), resulting in an almost complete decolorization of the solution. Moreover, during these time periods the intensity of the absorbance peaks due to the naphthalene and benzene rings also decreases, but with a lower rate compared to the azo absorption. After the complete decolorization of the solution, the absorbances corresponding to naphthalene and benzene rings remain practically unchanged, being almost negligible for the naphthalene rings. The fact that the intermediates with benzene rings did not completely disappear after the irradiation period

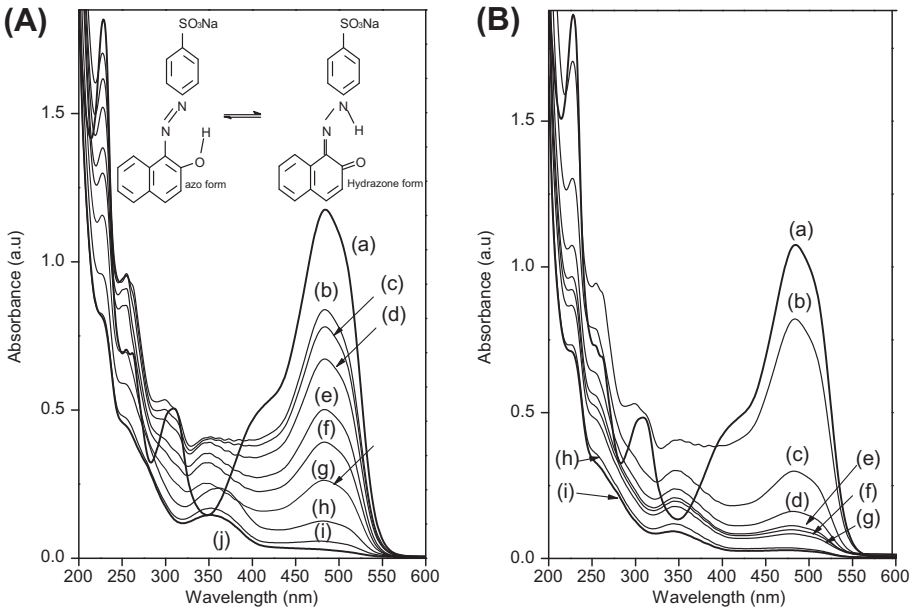


Fig. 11. UV–vis spectral changes of AO7 in aqueous solutions with the increase of irradiation time using TiO_2/Cr/MCM-41(3.5) A) under visible light: (a) Before addition of catalyst, (b) After equilibrium in dark, (c) 0.5 h, (d) 1 h, (e) 2 h, (f) 3 h, (g) 5 h, (h) 13 h, (i) 25 h and (j) 59 h and B) under UV–vis light: (a) Before addition of catalyst, (b) After equilibrium in dark, (c) 1 h, (d) 2 h, (e) 3 h, (f) 4 h, (g) 5 h, (h) 9 h, (i) 19 h.

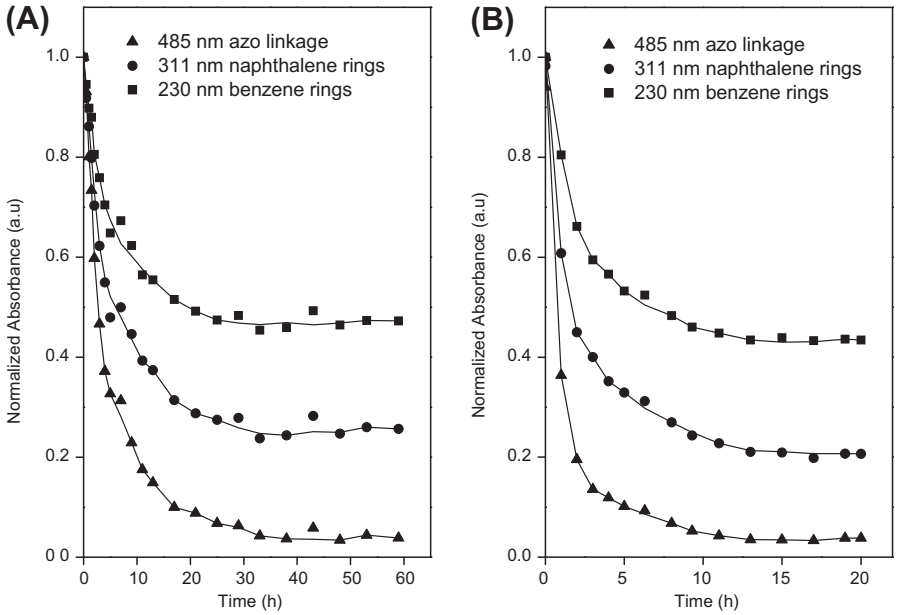


Fig. 12. Normalized absorbances of the main UV–vis bands of AO7 in aqueous TiO_2/Cr/MCM-41(3.5) suspension as functions of time of (A) visible and (B) UV–vis irradiation.

could be attributed to the formation of these by-products from the photodegradation of the azo dye and intermediate products containing naphthalene ring.

The intermediates species produced during the AO7 degradation under visible and UV–vis light were also examined with FT-IR and the infrared spectra are shown in Fig. 13. The spectrum corresponding to the initial AO7 solution (prior to the irradiation of light) presents several bands in the region of 2000–400 cm^{-1} which corresponds to different functional groups found in the AO7 molecule. According to literature, the band at 1509 cm^{-1} is usually assigned to the azo bond (–N=N–). The band at 1623 cm^{-1} is due to a combination of phenyl ring vibrations with stretching of the C=N group. The small band that appears at 1570 cm^{-1} is related to the NH–N=C group present in the hydrazone form of the AO7 molecule. The bands at 1597 and 1454 cm^{-1} are associated to aromatic C=C stretching vibrations also present in the dye molecule. Finally, it should be noted the presence of bands at 1198 cm^{-1} characteristic of $\upsilon_s(SO_3)$ and at 1123 and 1050 cm^{-1} due to the coupling between the benzene mode and $\upsilon_s(SO_3)$ [59]. The shoulder at 1258 and the band at 1220 cm^{-1} could be assigned to the υ(C–N) and υ(N–N) stretching vibrations, respectively [60]. Examining the FT-IR profiles corre-

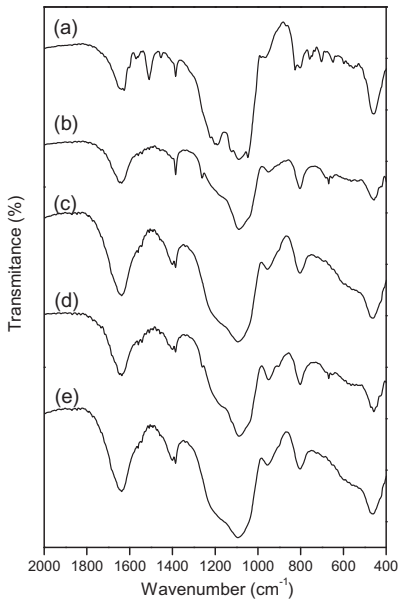


Fig. 13. Changes of FT-IR spectra during the photodegradation of AO7 over TiO_2/Cr/MCM-41(3.5): (a) Before irradiation, (b) After 5 h and (c) 20 h of visible irradiation and (d) After 5 h and (e) 20 h of UV–vis irradiation.

sponding to the AO7 solution under visible and UV–vis irradiation after 5 h of treatment, it can be observed that the band intensities characteristic of the azo bond (at 1509 cm^{-1}) and those associated to aromatic C=C stretching vibrations (1597 and 1454 cm^{-1}) decreased. These results are giving account for the degradation of both the parental dye and its primary aromatic breakdown products. Meanwhile, the disappearance of bands at 1198, 1123 and 1050 cm^{-1} of sulfonate also proved that the dye is being destroyed. Furthermore, it is notable that the band at 1258 cm^{-1} appears more defined probably due to the aromatic ammines produced by the dye degradation. After UV–vis irradiation ($X \sim 95\%$) the appearance of a band at 1405 cm^{-1}, associated to carboxyl groups, is indicating the oxidation of the aromatic rings where new intermediates with this functional group are being formed. The fact that this band is not observed after 5 h of visible irradiation indicates that in this case the degradation is slower than when UV–vis light is used. However, for longer periods of visible light irradiation, this band appears. This would indicate that the degradation process continues. In addition, the out-of-plane vibrations for the aromatic C–H are found between 700 and 900 cm^{-1}. These bands are frequently used to determine the degree and nature of substitution on the ring. Thus, the band at 760 cm^{-1}, assigned to four adjacent C–H bonds in the naphthalene ring, disappears after visible and UV–vis irradiation for 5 h which would be according to the negligible signal corresponding to naphthalene rings observed by UV–vis spectroscopy.

The evaluation of the mineralization of the dye using visible and UV–vis light was performed by measuring the TOC content of the samples. The TOC removal percentage obtained after 5 h of irradiation was around 25% (including the dye adsorption in the dark) under both visible and UV–vis light, where the AO7 decolorization percentage was around 80% and 95%, respectively. When the irradiation time was increased until the complete decolorization was reached ($X > 97\%$), the TOC removal slightly increased to around 35%.

Measurements of the biodegradability of the AO7 solutions were carried out to evaluate the capability of the photocatalytic oxidation process to be used as a pre-treatment step for effluents treatment. In order to express the biodegradability of the samples,

Table 2
X, COD, BOD_5 and biodegradability ratio (BOD_5/COD) values for several times of visible and UV–vis irradiation.

Sample	*X* (%)	COD (mg O_2/L)	BOD_5 (mg O_2/L)	BOD_5/COD
AO7: 20 ppm	–	27.63	0	0
After UV irradiation for 5 h	94.79	18.58	<2	0.11
After UV irradiation for 10 h	>97	16.40	7	0.43
After visible irradiation for 5 h	78.76	18.25	<2	0.11
After visible irradiation for 20 h	>97	17.40	9	0.52

the ratio BOD_5/COD is normally used [61,62]. Wastewater can be considered substantially biodegradable if it has a BOD_5/COD ratio between 0.4 and 0.8 [61,63]. The COD and BOD_5 of the samples before irradiation and at several irradiation times were measured and the obtained values are shown in Table 2. The ratio BOD_5/COD changes from 0 to 0.11 after 5 h of irradiation when the decolorization of the solution is around 80% and 95% under visible and UV–vis irradiation, respectively. However, when a complete AO7 degradation is reached ($X > 97\%$) the BOD_5/COD ratio increases to 0.52 and 0.43 after 20 and 10 h of visible and UV–vis irradiation, respectively. These results indicate that short irradiation periods lead to nonbiodegradable byproducts. Nevertheless, when longer irradiation times are applied, the biodegradability is enhanced by the photocatalytic oxidation converting nonbiodegradability organics into biodegradable forms. Also, the results evidence a relationship between decolorization and biodegradability, in which both the complete decolorization and the improvement of the biodegradability of wastewater dyes are achieved at the same time.

4. Conclusions

Well-ordered mesoporous MCM-41 silica were modified by the wet impregnation method with different Cr loadings and then with Ti. TEM images of these materials confirmed the presence of the hexagonal arrangement of unidirectional channels. SEM images do not reveal any particular crystalline morphology, although the spherical-like morphology seems to be the dominant for the Cr/MCM-41(x) samples and a partial aggregation was observed after the Ti loading. From the ESR results we could confirm the existence of Cr in higher oxidation states in the calcined catalysts and the increase of Cr^{3+} species with increasing Cr loading, also evidenced by XPS. Moreover, for the highest Cr loaded samples, the presence of a large proportion of Cr species inside the channels, corroborated by the results of TEM and XPS, would avoid the subsequent diffusion of Ti species and therefore the desired heterojunction. Meanwhile, the high dispersion of Cr species for the lower Cr loaded samples allows the further diffusion of Ti species inside the channels giving rise to an efficient interaction between the Cr^{6+} and Ti species. An AO7 decolorization of around 80% and 95% was reached after 5 h of visible and UV–vis irradiation, respectively, using the TiO_2/Cr/MCM-41(3.5) sample as catalyst. The analysis of the reaction progress, carried out by UV–vis and FT-IR spectroscopy, showed that short irradiation times result in a high degradation of the azo and naphthalene groups present in the AO7 dye. With respect to the biodegradability of the dye solution, the BOD_5/COD ratio was increased above 0.4 when the exposing time increased to 20 h and 10 h of visible and UV–vis irradiation, respectively, that are the times required for the complete decolorization. These results imply that the optimal exposing time for the photocatalytic process is the period needed for the complete decolorization. In this sense, the presented photocatalytic process could be employed as a pre-treatment step to improve the biodegradability of dye effluents.

Acknowledgments

This work was supported by the CONICET and UTN-FRC of Argentina. We gratefully acknowledge the support from MINCYT of Argentina and CONICYT from Chile through the project Cód CH/08/03 and from the Ministry of Science and Innovation, Spain (MICINN, Spain) through the project MAT2009-10481 and FEDER funds. The authors are grateful to Geol. Julio Fernandez for the IR spectra, Eng. Silvia Mendieta for the TEM and SEM images. M.L.S. also acknowledges Universidad Nacional del Litoral and Agencia Nacional de Promoción Científica y Tecnológica.

References

[1] E. Bizani, K. Fytianos, I. Poulios, V. Tsiridis, J. Hazard. Mater. 136 (2006) 85–94.
[2] http://www.cinu.org.mx/temas/des_sost/conf.htm.
[3] C. Guillard, J. Disdier, J. Dussaud, S. Malato, J. Blanco, M.I. Maldonado, J.M. Herrmann, Appl. Catal. B. 46 (2003) 319–332.
[4] H. Pinheiro, E. Touraud, O. Thomas, Dyes Pigm. 61 (2004) 121–139.
[5] C. Auer, A. Kalt, J. Photochem. Photobiol. A. 140 (2001) 87–92.
[6] M. Janus, Appl. Catal. B. 75 (2007) 118–123.
[7] P. Peralta-Zamora, C. Pereira, M. Rosa, R. Minussi, N. Durán, Appl. Catal. B. 42 (2003) 131–144.
[8] M. Neamtu, C. Zaharia, C. Catrinescu, A. Yediler, M. Macoveanu, A. Kettrup, Appl. Catal. B. 48 (2004) 287–294.
[9] M. Catanho, G. Malpass, A. Motheo, Appl. Catal., B. 62 (2006) 193–200.
[10] I. Konstantinou, T. Albanis, Appl. Catal. B. 49 (2004) 1–14.
[11] E. Bandala, M. Peláez, A. García-López, M. Salgado, G. Moeller, Chem. Eng. Process 47 (2008) 169–176.
[12] L. Davydov, E.P. Reddy, P. France, P.G. Smirniotis, J. Catal. 203 (2001) 157–167.
[13] E. Reddy, B. Sun, P. Smirniotis, J. Phys. Chem. B 108 (2004) 17198–17205.
[14] J.M. Herrmann, J. Disdier, P. Pichat, S. Malato, J. Blanco, Appl. Catal. B. 17 (1998) 15–23.
[15] V. Elías, E. Vaschetto, K. Sapag, M. Crivello, S. Casuscelli, G. Eimer, Top. Catal 54 (2011) 277–286.
[16] V. Elías, E. Vaschetto, K. Sapag, M. Oliva, S. Casuscelli, G. Eimer, Catal. Today 172–1 (2011) 58–65.
[17] V. Elías, E. Sabre, K. Sapag, S. Casuscelli, G. Eimer, Appl. Catal. A. 413–414 (2012) 280–291.
[18] G. Wang, L. Zhang, J. Deng, H. Dai, H. He, C.T. Au, Appl. Catal. A 1–2 (355) (2009) 192–201.
[19] S. Shylesh, P. Samuel, A. Singh, Appl. Catal. A 318 (2007) 128–136.
[20] T. Rao, Y. Yang, A. Sayari, J. Mol. Cat A. 301 (2009) 152–158.
[21] V. Elías, M. Crivello, E. Herrero, S. Casuscelli, G. Eimer, J. Non-Cryst. Solids 355 (2009) 1269–1273.
[22] Standard Methods for the Examination of Water and Wastewater, 20th ed, American Public Health Association/America Water Works Association/Water Environmental Federation, Washington DC, 1998.
[23] S. Rodrigues, S. Uma, I. Martyanov, K. Klabunde, J. Photochem. Photobiol. A 1–3 (165) (2004) 51–58.
[24] K. Choi, R. Wakabayashi, T. Tatsumi, T. Yokoi, K. Kuroda, J. Colloid Interface Sci. 359 (2011) 240–247.
[25] Y. Xu, G. Zhou, C. Wu, T. Li, H. Song, Solid State Sci. 13 (2011) 867–874.
[26] S. Ajaikumar, A. Pandurangan, Appl. Catal., A 357 (2009) 184–192.
[27] D. Yin, W. Li, W. Yang, H. Xiang, Y. Sun, B. Zhong, S. Peng, Microporous Mesoporous Mater. 47 (2001) 15–24.
[28] X. Hao, Y. Zhang, J. Wang, W. Zhou, C. Zhang, S. Liu, Microporous Mesoporous Mater. 88 (2006) 38–47.
[29] A. Bourlinos, A. Simopoulos, N. Boukos, D. Petridis, J. Phys. Chem. B 105 (2001) 7432–7437.
[30] D. Lensveld, J. Mesu, A. Van Dillen, K. de Jong, Microporous Mesoporous Mater. 44–45 (2001) 401–407.
[31] M. Hartmann, S. Racouchot, C. Bischof, Microporous Mesoporous Mater. 27 (1999) 309–320.
[32] Y. Cao, H. Wei, Z. Xia, Trans. Nonferrous Met. Soc. China 19 (2009) 656–664.
[33] S. Awate, N. Jacob, S. Deshpande, T. Gaydhankar, A. Belhekar, J. Mol. Catal. A 226 (2005) 149–154.
[34] I.-S. Park, S.Y. Choi, J.S. Ha, J. Khim, Chem. Phys Lett. 444 (2007) 161–166.
[35] T. Tsoncheva, S. Areva, M. Dimitrov, D. Paneva, I. Mitov, M. Linden, C. Minchev, J. Mol. Cat A. 1–2 (246) (2006) 118–127.
[36] M. Moreno, M. Weyland, P. Midgley, J. Bengoa, M. Cagnoli, N. Gallegos, A. Alvarez, S. Marchetti, Micron 37 (2006) 52–56.
[37] M. Betiha, S. Mahmoud, M. Menoufy, A. Al-Sabagh, Appl. Catal. B 3–4 (107) (2011) 316–326.
[38] L. Zhang, Y. Zhao, H. Dai, H. He, C.T. Au, Catal. Today 131 (2008) 42–54.
[39] M. Grün, K. Unger, A. Matsumoto, K. Tsutsumi, Microporous Mesoporous Mater. 27 (1999) 207–216.
[40] C. Chanquía, L. Andrini, J. Fernández, M. Crivello, F. Requejo, E. Herrero, G. Eimer, J. Phys. Chem. C 114 (28) (2010) 12221–12229.
[41] J. Mérida-Robles, M. Alcántara-Rodríguez, E. Rodríguez-Castellón, J. Santamaría-González, P. Maireles-Torres, A. Jiménez-López, Studies Surf. Sci. Catal. 130 (2000) 1865–1870.
[42] O. Gorriz, V. Cortes Corberin, J.G. Fierro, Ind. Eng. Chem. Res. 31 (1992) 2670–2674.
[43] J. Santamaría-González, J. Mérida-Robles, M. Alcántara-Rodríguez, P. Maireles-Torres, E. Rodríguez-Castellón, A. Jiménez-López, Catal. Lett. 64 (2000) 209–214.
[44] B. Weckhuysen, L. De Ridder, R. Grobet, R. Schoonheydt, J. Phys. Chem. 99 (1995) 320–326.
[45] M. Lezanska, G. Szymanski, P. Pietrzyk, Z. Sojka, J. Lercher, J. Phys. Chem. C 111 (4) (2007) 1830–1839.
[46] R. Puurunen, B. Weckhuysen, J. Catal. 210 (2002) 418–430.
[47] A. Morrish, The Physical Principles of Magnetism, IEEE, New York, 2001.
[48] D. Tobia, E. Winkler, R.D. Zysler, M. Granada, H. Troiani, Phys. Rev. B 78 (104412) (2008) 1–7.
[49] D. Tobia, E. Winkler, R. Zysler, M. Granada, H. Troiani, J. Alloys Compd. 495 (2010) 520–523.
[50] D. Cordischi, V. Indovina, M. Occhiuzzi, Appl. Surf. Sci. 4 (55) (1992) 233–237.
[51] S. Khaddar-Zine, A. Ghorbel, C. Naccache, J. Mol. Cat A. 1–2 (150) (1999) 223–231.
[52] S. Shylesh, C. Srilakshimi, A. Singh, B. Anderson, Microporous Mesoporous Mater. 99 (2007) 334–344.
[53] Y. Ohishi, T. Kawabata, T. Shishido, K. Takaki, Q. Zhang, Y. Wang, K. Takehira, J. Mol. Catal. A 230 (2005) 49–58.
[54] L. Liu, H. Li, Y. Zhang, Catal. Comm. 8 (2007) 565–570.
[55] N. Kawashima, N. Fujimoto, K. Meguro, J. Colloid Interface Sci. 103 (1985) 459–465.
[56] C. Bauer, P. Jacques, A. Kalt, J. Photochem. Photobiol. A. 140 (2001) 87–92.
[57] W. Feng, D. Nansheng, H. Helin, Chemosphere 41 (2000) 1233–1238.
[58] C. Galindo, P. Jacques, A. Kalt, J. Adv. Oxid. Technol. 4 (1999) 400–407.
[59] Y. Nie, C. Hu, J. Qu, X. Hu, J. Hazard. Mater. 154 (2008) 146–152.
[60] M. Stylidi, D. Kondarides, X. Verykios, Appl. Catal. B. 47 (2004) 189–201.
[61] E. Chamarro, A. Marco, S. Esplugas, Water Res. 35 (4) (2001) 1047–1051.
[62] J. Scott, D. Ollis, Environ. Prog. 14 (2) (1995) 88–103.
[63] F. Al-Momani, J. Degorce-Dumas, J. Roussy, O. Thomas, J. Photochem. Photobiol. A. 153 (2002) 191–197.